minerals

MDPI

Article

Modeling the Crystallization and Emplacement Conditions of a Basaltic Trachyandesitic Sill at Mt. Etna Volcano

Manuela Nazzari [1,2,*], Flavio Di Stefano [1], Silvio Mollo [1,2], Piergiorgio Scarlato [2], Vanni Tecchiato [1], Ben Ellis [3], Olivier Bachmann [3] and Carmelo Ferlito [4]

1 Department of Earth Sciences, Sapienza-Università di Roma, 00185 Rome, Italy; flavio.distefano@uniroma1.it (F.D.S.); silvio.mollo@uniroma1.it (S.M.); vanni.tecchiato@uniroma1.it (V.T.)
2 Istituto Nazionale di Geofisica e Vulcanologia, 00143 Rome, Italy; piergiorgio.scarlato@ingv.it
3 Department of Earth Sciences, Institute of Geochemistry and Petrology, ETH, 8092 Zurich, Switzerland; ben.ellis@erdw.ethz.ch (B.E.); olivier.bachmann@erdw.ethz.ch (O.B.)
4 Department of Biological, Geological and Environmental Sciences, University of Catania, 95129 Catania, Italy; cferlito@unict.it
* Correspondence: manuela.nazzari@uniroma1.it

Received: 9 January 2019; Accepted: 19 February 2019; Published: 21 February 2019

Abstract: This study documents the compositional variations of phenocrysts from a basaltic trachyandesitic sill emplaced in the Valle del Bove at Mt. Etna volcano (Sicily, Italy). The physicochemical conditions driving the crystallization and emplacement of the sill magma have been reconstructed by barometers, oxygen barometers, thermometers and hygrometers based on clinopyroxene, feldspar (plagioclase + K-feldspar) and titanomagnetite. Clinopyroxene is the liquidus phase, recording decompression and cooling paths decreasing from 200 to 0.1 MPa and from 1050 to 940 °C, respectively. Plagioclase and K-feldspar cosaturate the melt in a lower temperature interval of ~1000–870 °C. Cation exchanges in clinopyroxene (Mg-Fe) and feldspar (Ca-Na) indicate that magma ascent is accompanied by progressive H_2O exsolution (up to ~2.2 wt. %) under more oxidizing conditions (up to ΔNNO + 0.5). Geospeedometric constraints provided by Ti–Al–Mg cation redistributions in titanomagnetite indicate that the travel time (up to 23 h) and ascent velocity of magma (up to 0.78 m/s) are consistent with those inferred for other eruptions at Mt. Etna. These kinetic effects are ascribed to a degassing-induced undercooling path caused principally by H_2O loss at shallow crustal conditions. Rare earth element (REE) modeling based on the lattice strain theory supports the hypothesis that the sill magma formed from primitive basaltic compositions after clinopyroxene (≤41%) and plagioclase (≤12%) fractionation. Early formation of clinopyroxene at depth is the main controlling factor for the REE signature, whereas subsequent degassing at low pressure conditions enlarges the stability field of plagioclase causing trace element enrichments during eruption towards the surface.

Keywords: sill magma; magma decompression and degassing; REE fractionation; Mt. Etna volcano

1. Introduction

Mt. Etna volcano (Sicily, Italy; Figure 1a) is the largest volcano in Europe, and one of the most active and most intensely monitored on Earth. The volcanic edifice is 1200 km^2 wide and 3.3 km high. The greater part of the stratovolcano was constructed by overlapping products with a Na-alkaline affinity and principally erupted in the last 220 ka (e.g., Reference [1]). Magma dynamics are frequently referred to the pulsatory upward migration of H_2O-rich magmas and/or fluxes of abundant volatiles from depth [2–6]. The explosive activity of the volcano mostly involves gas-charged

magmas formed at mantle depths with primitive compositions [7,8]. However, distinct magma storage regions at deep, intermediate and shallow levels have been recognized along the vertically-developed plumbing system [9–15]. The migration of magma towards the surface changes its physicochemical state, thus controlling mineral and melt compositions, degree of crystallization, magma ascent velocity and type of eruption [2,9,10,16–20]. A distinctive feature of the recent activity (post-1971) is the persistent eruption of magmas with K-affinity and buffered to trachybasaltic compositions that sporadically evolve towards basaltic trachyandesites [21]. In contrast, historic (pre-1971) and prehistoric products show a distinctive Na-affinity, ranging from hawaiites to mugearites. The Valle del Bove (Figure 1b) volcanic succession is characterized by a rarity of primitive products and its prehistoric eruptions evolve up to trachyte encompassing high degrees of crystallization (>40%). This remarkable compositional variability has been attributed to crystal fractionation processes at shallow crustal levels mostly controlled by degassing and H_2O exsolution phenomena [16,22–25].

In this study, we present new geochemical data from a sill (~80 m long and ~30 m thick; Figure 1c) at ~1780 m altitude in the southern wall of the Valle del Bove (Figure 1b). The intrusive body is in continuity with the prehistoric lava flows of Trifoglietto (80–60 ka) and Ellittico (60–15 ka) eruptive centers [26]. The sill is in sharp contact with the host lavas and its age is therefore constrained as post flow emplacement. The exposure is 80 m long, but the sill continues buried out of sight. Nine rock samples have been collected at the central portion of the sill using a sampling distance of 1.5 m. Major and trace elements of bulk rocks and single minerals have been analyzed for each rock sample and then discussed in the framework of magma modeling based on P–T–fO_2–H_2O-lattice strain equations. This approach constrains the crystallization and emplacement conditions of the sill, illustrating that the differentiation of prehistoric magmas started at intermediate (~6 km) depths [27–30] and proceeded through fractional crystallization, degassing and cooling phenomena at shallow crustal levels or during ascent towards the surface (e.g., References [16,24,25]).

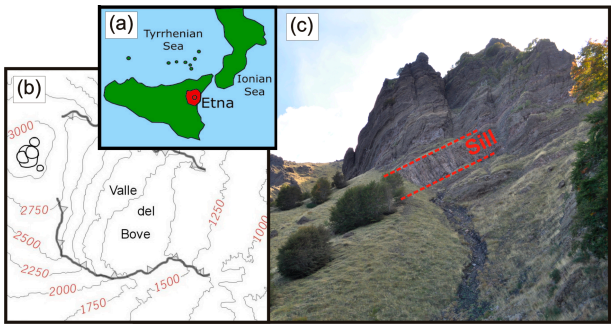

Figure 1. Schematic map showing the location of Mt. Etna volcano (**a**), Valle del Bove depression (**b**) sill formation (**c**).

2. Methods

Photomicrographs of the sill samples were collected with the backscattered electron (BSE) mode of a field emission gun-scanning electron microscopy (FE-SEM) Jeol 6500F (JEOL, Ltd., Tokyo, Japan) equipped with an energy-dispersive spectrometer (EDS) detector and installed at the HPHT Laboratory of Experimental Volcanology and Geophysics of the Istituto Nazionale di Geofisica e Vulcanologia (INGV) in Rome, Italy.

Microchemical analyses of minerals were performed at the INGV with a JEOL-JXA8200 electron probe microanalyzer (EPMA, JEOL, Ltd., Tokyo, Japan) equipped with five spectrometers. The crystals were analyzed using 15 kV accelerating voltage and 10 nA beam current, with a beam size of 2 μm and counting time of 20 and 10 s on peaks and background, respectively. The following standards were adopted: Jadeite (Si and Na), labradorite (Al and Ca), forsterite (Mg), andradite (Fe), rutile (Ti), orthoclase (K), barite (Ba), apatite (P) and spessartine (Mn). Sodium and potassium were analyzed first to prevent alkali migration effects. The precision of the microprobe was measured through the

analysis of well-characterized synthetic oxides and minerals. Data quality was ensured by analyzing standard materials as unknowns. Based on counting statistics, analytical precision was better than 5% for all cations.

Major elements of bulk rocks were measured at the Institute of Geochemistry and Petrology of the ETH Zürich, Switzerland. For the chemical analyses, 1.5 g of powdered sample was heated to 950 °C for 2 h in a chamber furnace and then weighed to determine the loss on ignition (LOI). The ignited material was charged in a Pt-Au crucible and fused with a 1:5 lithium–tetraborate mixture using a Claisse M4® fluxer. The fused disk was analyzed for major elements using a wave-length dispersive X-ray fluorescence spectrometer (WD-XRF; Axios PANanalytical, Malvern Panalytical Ltd., Malvern, UK) equipped with five diffraction crystals. Calibration was based on thirty certified international standards of predominantly igneous and metamorphic rocks.

Trace element analyses of both bulk rock disks and minerals (i.e., clinopyroxene and plagioclase) were performed at ETH Zürich through a 193 nm excimer laser coupled with a second generation two-volume constant geometry ablation cell (Resonetics: S-155LR) and a high-sensitivity, sector-field inductively-coupled plasma mass spectrometer (ICP-MS; Thermo: Element XR). Points with a spot size of 30 μm (producing laser depth crater of 15 μm) were set on chemically homogeneous portions of the material and ablated with a pulse rate of 10 Hz and an energy density of 3.5 J/cm^3 for 40 s. The isotopes were analyzed relative to an external standard of known composition (i.e., NIST612). A second standard (i.e., GSD-1G) was used as an unknown to check the quality of data during each analytical run. ^{43}Ca was adopted as an internal standard, in order to recover the concentrations of light and heavy rare earth elements (REE divided in LREE and HREE). The 1 sigma errors calculated from variations in replicate analyses were invariably several times larger than the fully integrated 1 sigma errors determined from counting statistics alone. Potential mineral/melt contamination phenomena are excluded following the data reduction method reported in Reference [31]. Concentration calculation of transient laser ablation signals where performed by selecting segments of time corresponding to when the laser was ablating through a homogeneous vertical section of a sample (i.e., the time-resolved signals of all the elements are parallel). Through this criterion the ratios of all elements analyzed are constant with time. In contrast, cross-cutting time-resolved elemental curves indicate a transition into a new material and contamination phenomena. In this case, the laser ablation signal is not considered. In order to further verify the quality of the laser data, some key mineral-melt partition coefficients have been also calculated and compared with those from literature. Similar values have been found, attesting the reliability of the data (see discussion below).

3. Results

3.1. Texture

The most important petrographic features observed for the nine sill samples are summarized in Figure 2. The rock samples are poorly vesicular (<3%) with porphyritic index (PI = the total phenocrysts content) variable from 35 to 40, in agreement with the typical phenocryst content of prehistoric and historic (pre-1971) lava flows [13,23,32]. Phenocrysts, microphenocrysts and microlites are discriminated on the basis of the longest size dimensions >0.3, 0.3–0.1, and <0.1 mm, respectively [33,34]. The phenocryst and microphenocryst assemblage consist of plagioclase (43 vol. %), clinopyroxene (40 vol. %), alkali feldspar (11 vol. %), and titanomagnetite (6 vol. %), in order of abundance. Glomerocrysts of clinopyroxene, plagioclase and titanomagnetite are also frequent [19]. The habit of large clinopyroxene phenocrysts is prismatic with well-formed planar edges that may enclose small, sub-rounded titanomagnetites (Figure 2). In terms of maximum abundance and crystal size, clinopyroxene dominates the mineral association of glomerocrysts, suggesting early crystallization as liquidus phase [35]. Moreover, no evident disequilibrium textures are found, such as dendritic morphologies typical of rapid growth conditions [36]. On the other hand, large titanomagnetites and plagioclase preferentially develop as isolated crystals. The growth of titanomagnetite proceeds through

the aggregation and coalescence of smaller and mutually touching microlites, resembling the textural maturation documented during magma undercooling phenomena [37]. In contrast, the crystal habit of feldspars is generally tabular (Figure 2) and a great number of tiny titanomagnetite crystals may be entrapped in the larger plagioclase phenocrysts.

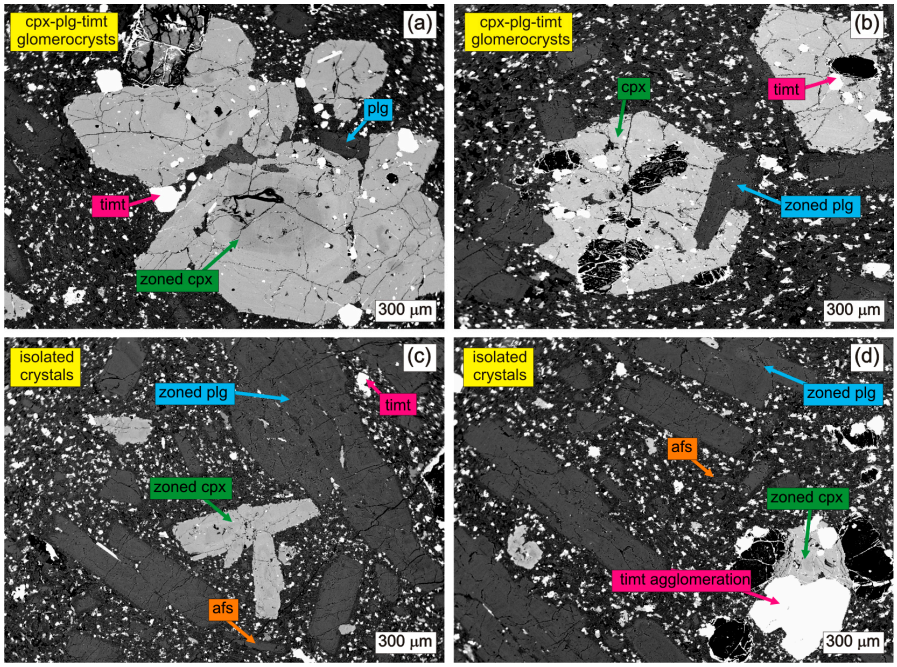

Figure 2. Petrographic features observed for the sill samples and evidencing the occurrence of either glomerocrysts (**a**,**b**) of clinopyroxene, plagioclase and titanomagnetite or isolated crystals (**c**,**d**). Clinopyroxene and plagioclase are normally zoned, whereas large titanomagnetite phenocrysts form by the attachment and agglomeration of smaller crystals. Alkali feldspar occurs only as microphenocryst. Cpx, clinopyroxene. Plg, plagioclase. Afs, alkali feldspar. Timt, titanomagnetite.

3.2. Mineral Chemistry

Major oxide and trace element analyses of clinopyroxene, plagioclase, alkali feldspar and titanomagnetite from this study are reported in Tables S1–S4 submitted as Supplementary Materials. No clear chemical variations are observed for minerals collected from the uppermost to the lowermost part of the sill.

The site occupancies, molecular components, and Fe^{3+}/Fe^{2+} ratios of clinopyroxene have been calculated on the basis of six oxygen atoms following References [38,39]. Crystals are zoned with more magnesian cores (74–84 Mg#, where Mg# is the molar ratio of Mg to Mg + Fe_{tot}) relative to mantles and rims (69–83 Mg#). Using the classification scheme of Reference [40], clinopyroxenes cores are diopside, whereas more evolved mantles and rims are diopside-augite (Figure 3a). Major cations incorporated in clinopyroxene vary systematically from core to rim, showing enrichments in ^{T}Al (0.04 to 0.21 apfu), Fe^{3+} (0.01 to 0.16 apfu) and Ti (0.01 to 0.04 apfu), counterbalanced by depletions in Mg (0.91 to 0.75 apfu) and Ca (0.90 to 0.72 apfu). Intriguingly, clinopyroxene phenocrysts are characterized by ^{T}Al contents (0.04–0.17 apfu) higher than ^{M1}Al concentrations (0.01–0.1 apfu), possibly responding to low pressure crystallization conditions [41,42]. These cation redistributions cause the sum of diopside (Di) plus hedenbergite (Hd) to progressive decreases from core (0.84 mol. % DiHd) to rim (0.76 mol. % DiHd), whereas the tschermakitic components (ΣTs equals to the sum of CaTs and CaFeTs and CaTiTs, where Ts refers to the Tschermak molecule) increase from 0.04 to 0.17 mol. %. The Tschermak-rich crystal portions result from the coupled substitution ^{T}Al with Si and ^{M2}(Mg, Fe^{2+}) with ^{M1}(Al, Fe^{3+}), as well as CaFe- and CaTi-Tschermak molecular increment compensates the decrement of ^{M1}Al with Fe^{3+} [35,43]. The chondrite-normalized pattern [44] of REE (Figure 4a) exhibits sub-parallel trends

shifting towards progressive REE enrichments from core to rim. The apparent preferential enrichments for HREE relative to LREE are also consistent with those observed for diopside-augite clinopyroxenes from prehistoric Etnean eruptions at Valle del Bove (cf. [45,46]). The crystal cores show weak negative europium anomalies (0.87–0.99 Eu/Eu^{*}) that are more evident at the crystal rims (0.71–0.87 Eu/Eu^{*}). The LREE/HREE ratio also increases from core (3.22 La_N/Yb_N) to rim (6.51 La_N/Yb_N).

Plagioclase exhibits a pronounced normal zoning and its composition shifts from labradorite to andesine in the ternary feldspar diagram (Figure 3b). Grading from core to rim, the amount of anorthite (An) decreases remarkably from 0.67 to 0.56 mol. %, whereas orthoclase (Or) slightly increases from 0.02 to 0.04 mol. % (formula on the basis of 8 oxygens). Major cations gradually change during crystal growth, with Ca (0.13 to 0.09) and Fe (0.011 to 0.003 apfu) depletions associated with Na (0.06 to 0.11 apfu) and K (0.004 to 0.008 apfu) enrichments. The mineral stoichiometry is evidence of Fe increase with increasing An [47,48]. Rationally, a lower number of Si cations leaves larger available T- and M-sites for Fe substitution with increasing An [49–53]. The pattern of REE shows a marked positive europium anomaly (7.21–17.91 Eu/Eu^{*}; Figure 4b) similar to that observed for several Etnean eruptions [54]. Plagioclase is preferentially enriched in LREE with respect to HREE (Figure 4b), and the LREE/HREE ratio increases from core (243 La_N/Yb_N) to rim (740 La_N/Yb_N).

The alkali feldspar is characterized by core to rim compositions variable from anorthoclase to sanidine (Figure 3b). Due to its small crystal size, both microphenocryst mantle and rim compositions overlap at the scale of the microprobe analysis. The concentration of An decreases from 0.12 to 0.04 mol. % during crystal growth, whilst substantial Or enrichments are measured from 0.25 to 0.50 mol. %. As for the case of plagioclase, the amount of Fe (0.004–0.007 apfu) in alkali feldspar scales with the concentration of An. From core to rim, the proportion of K increases remarkably from 0.05 to 0.12 apfu, at the expense of Na content.

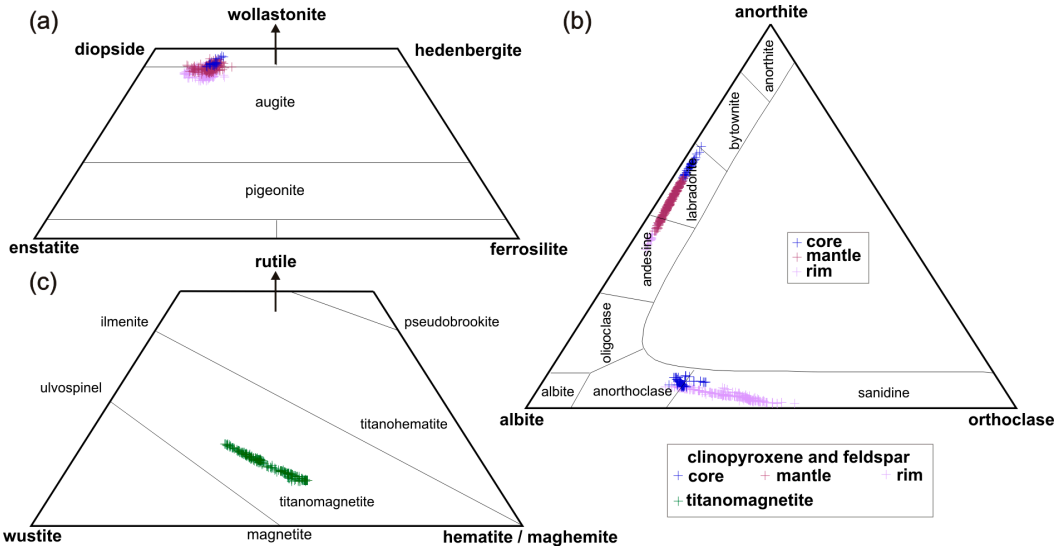

Figure 3. Classification diagrams used for clinopyroxene (**a**), feldspar (**b**) and titanomagnetite (**c**). The site occupancies, molecular components, and Fe^{3+}/Fe^{2+} ratios of clinopyroxene have been calculated on the basis of six oxygen atoms following References [38,39], whereas the classification scheme adopted comes from Reference [40]. The stoichiometry and composition of magnetite (Mt)-ulvospinel (Usp) solid solution has been recalculated following Reference [55].

Titanomagnetite is the only opaque mineral present in the sill samples. The stoichiometry and composition of magnetite (Mt)-ulvospinel (Usp) solid solution has been recalculated following Reference [55]. The TiO_2-FeO-$1/2Fe_2O_3$ ternary diagram shows that the Usp content of titanomagnetite decreases from 0.60 to 0.38 mol. % (Figure 3c). When the crystal is depleted in Ti, higher Fe^{3+}/Fe^{2+} ratios (0.47 to 95) are determined on the basis of stoichiometric and charge balance criteria. Enrichments

in Al (0.08 to 0.17 apfu) and Mg (0.06 to 0.15 apfu) are also evident, resembling those observed during magma undercooling and cooling rate conditions [37,56].

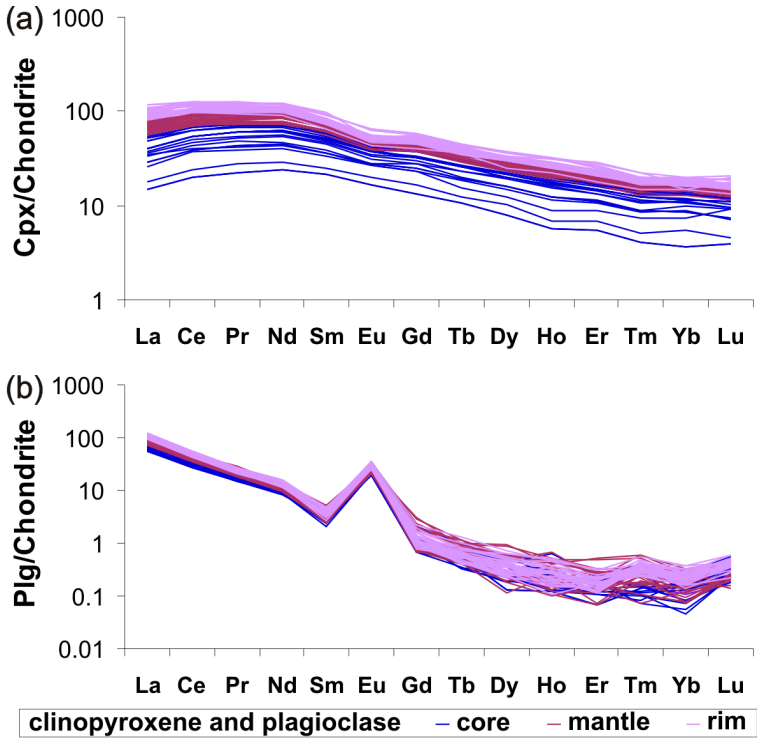

Figure 4. Chondrite-normalized patterns [44] of REE showing the trace element concentrations analyzed in clinopyroxene (**a**) and plagioclase (**b**).

3.3. Bulk Rock Geochemistry

Major oxide and trace element analyses of bulk rocks from this study are reported in Table S5 submitted as Supplementary Materials. In the TAS (total alkali vs. silica; [57] diagram (Figure 5a), the sill bulk rocks are classified as basaltic trachyandesites (i.e., mugearites), with compositions intermediate between those of trachybasalts and trachyandesites characterizing the Etnean products at Valle del Bove depression [22,23,25,26,58]. In terms of SiO_2 and Mg#, the chemical analyses slightly shift from ~54 to ~55 wt. % and ~40 to ~49 wt. %, respectively, perhaps responding to minor changes in the mineral proportions. The chondrite-normalized patterns [44] of REE are markedly homogeneous, exhibiting sub-parallel trends with LREE enrichments relative to HREE (Figure 5b). REE concentrations generally increase with increasing SiO_2, reproducing patterns typical of Etnean alkaline suites [23,24,32]. Bulk rocks are also characterized by weak negative Eu anomalies (0.83–0.96 Eu/Eu^*; Figure 5b) and relatively high LREE/HREE ratios (20–29 La_N/Yb_N).

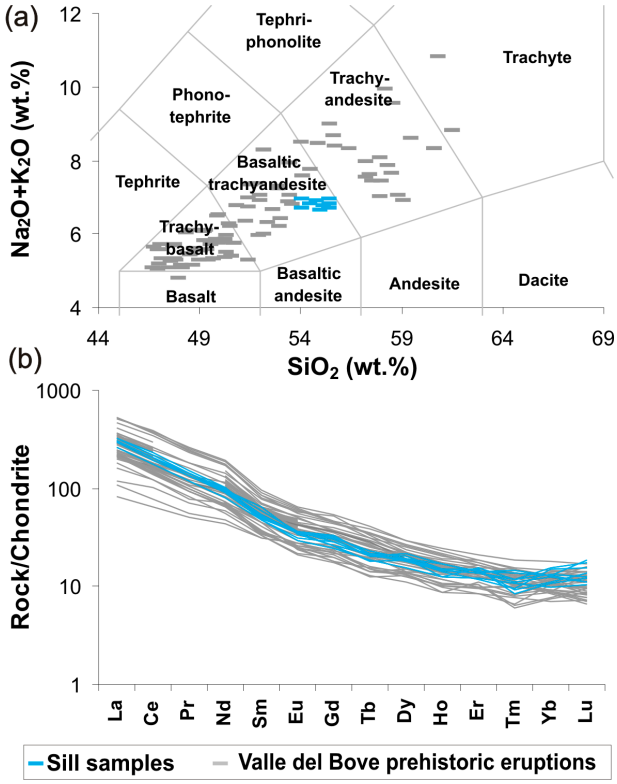

Figure 5. TAS (total alkali vs. silica; [57] diagram (**a**) and chondrite-normalized patterns [44] of REE (**b**) showing the sill bulk rock compositions.

4. Discussion

4.1. Identifying the Equilibrium Mineral Compositions

In natural Etnean products the occurrence of residual melts is extremely rare, due to abundant crystallization of matrix minerals at both syn- and post-eruptive conditions (e.g., Reference [18]). Therefore, it may be difficult to correctly recognize the chemical correspondence between a zoned mineral and the melt from which it crystallized. Under such circumstances, the intensive variables of the system are estimated through the application of petrological models by assuming that the bulk rock analysis corresponds to the original magma composition feeding the crystal growth [17,19,59]. However, this strategy cannot be safely applied when the investigated crystal compositions are not in equilibrium with the host magma. This is especially true for the Etnean plumbing system where the transfer of magma through several compositionally different sub-volcanic environments frequently occurs [12,15]. The activity of Mt. Etna is characterized by a highly dynamic regime with continuous recharge of the volcanic conduit by rapid input of new magma batches. Under such dynamic conditions, the crystal growth is strongly influenced by volatile loss (i.e., degassing) and heat dissipation (i.e., cooling), due to slow to moderate degrees of undercooling experienced by magma [13,19,60,61]. In particular, the occurrence of zoned phenocrysts (Figures 2 and 3) testifies to cation exchange reactions at the crystal-melt interface that are controlled by kinetic pathways in which the crystal composition changes upon the effect of an ever-changing *P*-*T*-H_2O path bounded between the mineral saturation temperature and the closure temperature for crystal growth [13,62]. The primary effect related to the lack of equilibrium is that thermometers, barometers, and hygrometers based on mineral-melt or mineral-mineral equilibrium are affected by great uncertainties, up to one order of magnitude higher than the calibration errors of the models [35,36,53,63]. To obviate this issue and correctly estimate the crystallization conditions of the sill, the compositions of the clinopyroxene,

plagioclase, alkali feldspar and titanomagnetite have been tested for equilibrium with the host magma through the application of some experimentally-derived models from literature.

In order to decipher the equilibrium compositions of clinopyroxene phenocrysts, we have adopted the model of Reference [35] based on the difference (Δ) between DiHd components predicted for clinopyroxene via regression analyses of clinopyroxene-melt pairs in equilibrium conditions, with those measured in the analyzed crystals. ΔDiHd equals to zero only at thermodynamic equilibrium, but values lower than 0.1 may, with caution, attest near-equilibrium crystallization (cf. [64]). For the sill samples, most of the clinopyroxene core-to-rim compositions approach to the one-to-one line of the DiHd measured vs. DiHd predicted plot (Figure 6a), a feature that is not surprising considering that clinopyroxene is the liquidus phase and its early growth is fed by the original magma composition (i.e., the bulk rock analysis). The attainment of equilibrium crystallization is also corroborated by the lattice strain model of Reference [65] for the partitioning of Ti (D_{Ti}) between clinopyroxene and melt. This is a thermodynamically-derived equation based on the electrostatic work done by placing a tetravalent cation in a charge-balanced/imbalanced clinopyroxene site, and the electrostatic effect produced by insertion of the same cation in the melt, as described in Reference [66]. Most of the values of D_{Ti} predicted by the model of Reference [65] are similar to those measured from this study (Figure 6b), denoting that the growth of clinopyroxene was not affected by kinetically-controlled phenomena or marked degrees of undercooling. During rapid clinopyroxene growth, Al in the tetrahedral site is incorporated at disequilibrium proportions [36,67] and highly charged cations, such as Ti, are preferentially accommodated in the M1 site of clinopyroxene (i.e., D_{Ti} deviates from the equilibrium condition) to balance the charge deficiency caused by the increasing concentration of ^{T}Al [45,68]. The close correspondence between near-equilibrium ΔDiHd values (Figure 6a) and the partitioning behavior of Ti (Figure 6b) confirms the relationship between the cation exchange [^{T}Si, ^{M2}(Mg, Fe^{2+})] ↔ [^{T}Al, ^{M1}(Al, Fe^{3+})] and the accommodation of Ti in the M1 site of clinopyroxene. Disequilibrium cation incorporations are also excluded by the Fe–Mg exchange, showing values (0.24–0.26) within the equilibrium ranges of 0.27 ± 0.03 and 0.28 ± 0.08 derived by Reference [69] and Reference [59], respectively.

With respect to plagioclase crystallization, the An-based model of Reference [70] suggests equilibrium compositions between An_{46} and An_{59}, corresponding to the mantle analyses of plagioclase (Figure 6c). Evidently, plagioclase saturation took place after substantial clinopyroxene fractionation, as indicated by the europium anomaly (71–81 Eu/Eu^{*}) measured at clinopyroxene rim. Moreover, the La/Eu ratio in clinopyroxene is ~1–9 at the early stage of crystallization. Conversely, further crystallization from a more differentiated melt leads the La/Eu ratio to increase in plagioclase up to ~19, thus identifying substantial enrichment in LREE during magma evolution. The Ca–Na exchange model of Reference [71] yields equilibrium values between 1.15 and 1.7 (Figure 6d). Despite the An content of plagioclase is positively correlated with H_2O and temperature, the Ca–Na exchange is mostly a proxy for the amount of H_2O dissolved in the melt, provided that the effects of temperature and pressure are negligible for the equilibrium (cf. [72]). Looking at the experimental data of Reference [73], it is interesting to note that the measured values of Ca–Na exchange translate to a range of 0–2 wt. % H_2O [11,13,17,74] typically measured for Etnean degassing magmas (see below).

The feldspar activity model of Reference [59] indicates that plagioclase and alkali feldspar cosaturation refers to the An-rich portions of the crystals aligning along the one-to-one line (Figure 6e). The chemical evolution of sanidine (Figure 2b) requires enrichments in Or component and is driven by alkali-rich melts that develop at the late stage of magma differentiation. The Or–Ab exchange (3.8–1.4) calculated with the model of Reference [20] specific to anorthoclase and sanidine, confirms equilibrium crystallization from more differentiated melts characterized by increasing K_2O concentrations.

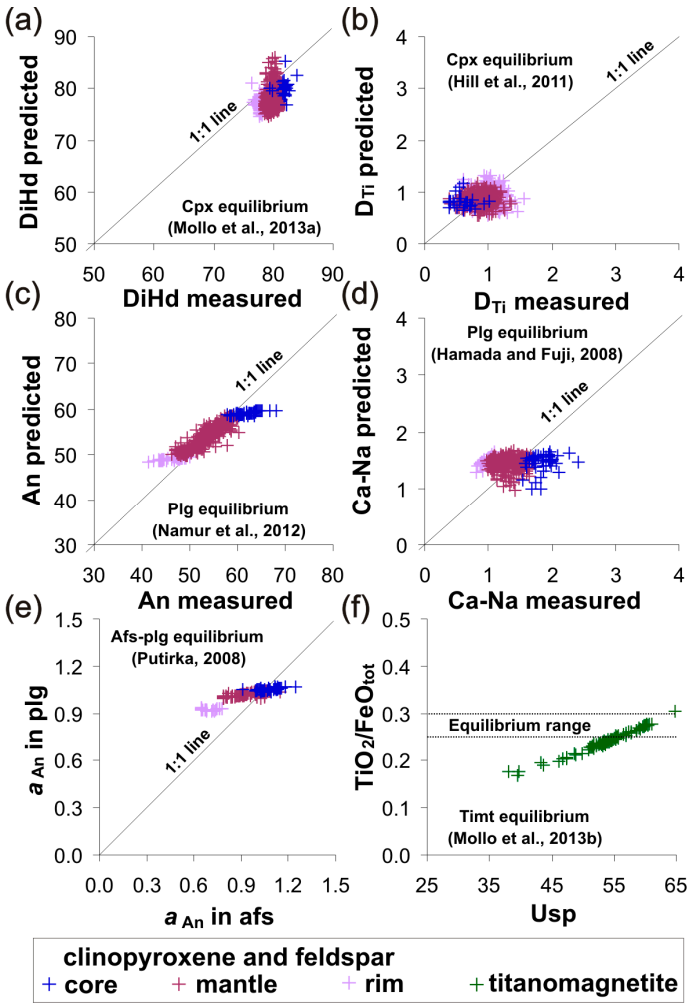

Figure 6. Test for equilibrium between the bulk rock analysis (i.e., the original magma composition) and clinopyroxene (**a**,**b**), feldspar (**c**–**e**) and titanomagnetite (**f**). The DiHd (diopside + hedenbergite) model comes from Reference [35] with an equilibrium range 0–0.1. The partitioning of Ti (D_{Ti}) between clinopyroxene and melt is predicted by the lattice strain equation of Reference [65]. An (anorthite) in plagioclase is predicted by the thermodynamically-derived expression of Reference [70]. The Ca–Na exchange model comes from Reference [71]. The feldspar activity model (i.e., the activity of anorthite in plagioclase and alkali feldspar) has been derived by Reference [59]. The TiO_2/FeO_{tot} equilibrium range between 0.25 and 0.30 has been experimentally-measured by Reference [37].

Titanomagnetites from the sill samples explore important compositional variations. The experimental study of Reference [37] demonstrates that Etnean magmas equilibrate with titanomagnetites showing TiO_2/FeO_{tot} ratio between 0.25 and 0.30 (Figure 6f). Within this equilibrium range, the Usp contents of phenocrysts and microphenocrysts from the sill samples are consistent with values commonly measured for magmatic intrusions, lava flows and lava fountains at Mt. Etna volcano [42,75]. Otherwise, the TiO_2/FeO_{tot} ratio substantially decreases when Ti is less favorably incorporated into the titanomagnetite crystal lattice upon the effect of increasing undercooling conditions [37,56].

4.2. Retrieving the Crystallization Conditions of Magma

The oxygen fugacity of the sill magma has been estimated through the titanomagnetite-based oxygen barometer (error ±0.5 log unit) of Reference [76], integrating the Fe^{2+}-Fe^{3+} partitioning between spinel and melt [77] with the Fe^{3+}/Fe^{2+} ratio and fO_2 [78]. Figure 7 shows that titanomagnetite crystals

formed under buffering conditions variable from ΔNNO − 0.4 to ΔNNO + 0.4 (where NNO refers to the nickel-nickel oxide equilibrium reaction). This range is comparable to that measured by other independent models applied to a variety of Etnean products [11,13,17,25,42,79]. As a further test, the formulation of Reference [80] has been also adopted to derive the oxygen fugacity of the sill magma. This is a logarithmic relationship (error ±0.1 log unit) relating the redox state of iron in the melt with the anorthite content in plagioclase. The model predicts redox conditions comprised between ΔNNO − 0.1 and ΔNNO + 0.5 (Figure 7), paralleling the fO_2 trend of titanomagnetite and possibly indicating feldspar-spinel cosaturation at the time of sill solidification.

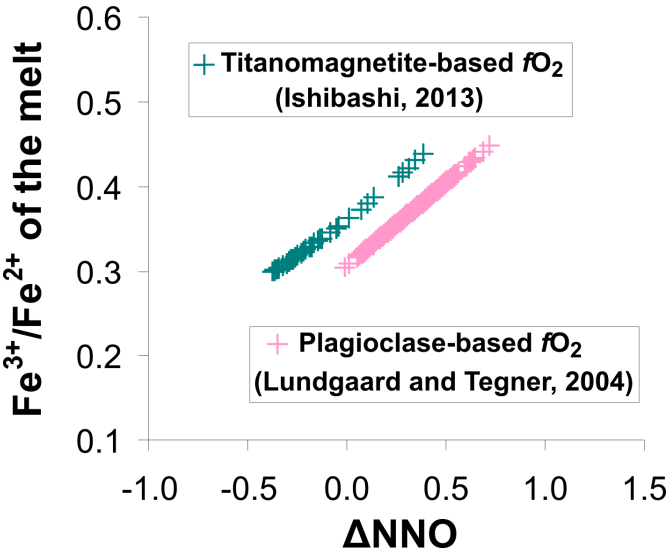

Figure 7. Oxygen fugacity of the sill magma estimated by (1) the titanomagnetite-based oxygen barometer (error ±0.5 log unit) of Reference [76], integrating the Fe^{2+}-Fe^{3+} partitioning between spinel and melt [77] with the Fe^{3+}/Fe^{2+} ratio and fO_2 [78], and (2) the formalism of Reference [80], relating the redox state of iron in the melt (error ±0.1 log unit) with the anorthite content in plagioclase.

The crystallization temperatures and pressures of clinopyroxene phenocrysts have been calculated by the H_2O-independent thermometer (error ±28 °C) and barometer (error ±150 MPa) of Reference [39] and Reference [69], recently refined for alkaline magmas by Reference [62]. The estimates, plotted in Figure 8a, show that the saturation surface of clinopyroxene progressively decreases from ~1050 to ~934 °C along a decompression path from ~198 to ~0.1 MPa. The early crystallization temperature of the sill magma agrees with the thermal range of 1050–1080 °C documented by direct measurements of inner lava flow temperatures [81]. The overall thermal path is also similar to the crystallization conditions of 1075–875 °C derived for prehistoric and historic lava flows at Mt. Etna volcano [75]. The relative low pressure range, displayed in Figure 8a, conforms to geophysical observations of magma bodies stored at intermediate (~6 km) depths [27–30], as well as the preferential incorporation of ^{T}Al into clinopyroxene crystal lattice relative to ^{M1}Al [41,42]. This cation exchange is generally addressed to magma crystallization under H_2O-saturated conditions, as experimentally observed for Etnean compositions by Reference [82]. According to a number of studies [4,14,15,17,46,83], the amount of H_2O dissolved in the melt is a key parameter controlling the crystallization behavior and ascent rate of magmas at Mt. Etna. To calculate melt-H_2O contents of the sill, the clinopyroxene-based hygrometer (error ±0.5 wt. % H_2O) of Reference [84] has been employed in concert with the independent estimates of temperature and pressure reported above. Figure 8b shows that H_2O concentration progressively decreases from ~2.1 to 0 wt. % as pressure decreases. Most of the H_2O loss occurs at P < 100 MPa, in agreement with melt inclusion data attesting as strong degassing takes place during magma ascent towards very shallow crustal levels [2,85,86]. A decreasing melt-H_2O content is also derived by SolEx solubility model [87], yielding a conservative H_2O content of ~1 wt. % that is exsolved from the

melt only at P < 25 MPa [13,19,60]. Although H_2O exsolves with decreasing pressure, ascending magmas at Mt. Etna can retain part of their original volatile content with the result of abundant degassing at post-emplacement conditions [88]. As demonstrated by Reference [17] and Reference [84], the composition of clinopyroxene is a valuable tool to track the degassing path of Etnean magmas, accounting for the dependence of Jd-DiHd and CaTs-DiHd exchange equilibria to the melt-H_2O content. There is a positive correlation between the Fe/Mg ratio of clinopyroxene and the amount of H_2O dissolved in the melt [89]. Thermodynamic calculations reported in Reference [90] show that H_2O reduces the activity of MgO relative to FeO in the melt according to the reaction: $Fe(OH)_2 + MgO \rightarrow Mg(OH)_2 + FeO$. Through the application of the stoichiometric formalism of Reference [38], it is found that Fe^{2+} in clinopyroxene is positively correlated with the amount of H_2O (Figure 8c), thus confirming that hydroxyl groups formed complexes with Mg^{2+} rather than Fe^{2+} during ascent and emplacement of the sill magma.

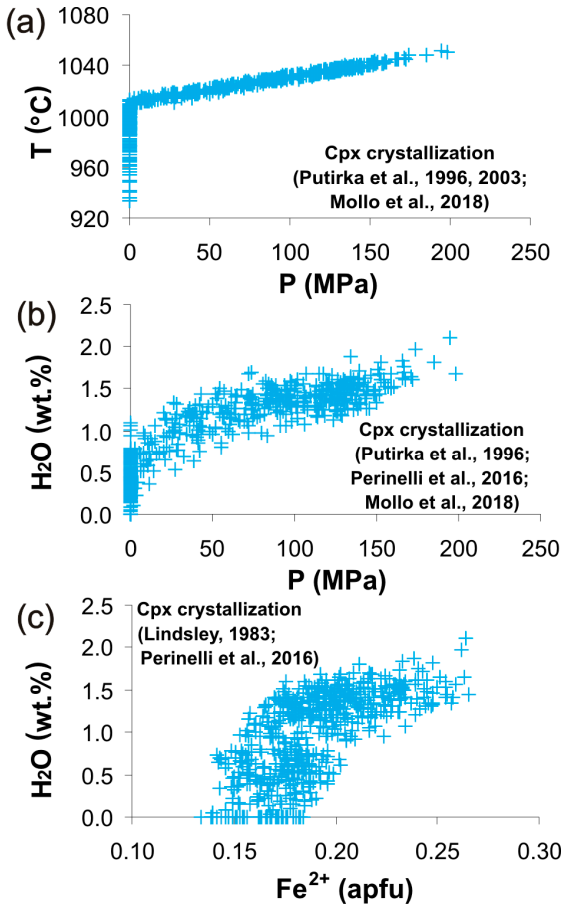

Figure 8. Temperatures (**a**), pressures (**a**,**b**) and melt-H_2O contents (**b**,**c**) in equilibrium with clinopyroxene phenocrysts have been estimated by the H_2O-independent thermometer (error ±28 °C) and barometer (error ±150 MPa) of Reference [39], Reference [69], recently refined for alkaline magmas by Reference [62], as well as the hygrometer (error ± 0.5 wt. % H_2O) of Reference [84]. The Fe^{2+} in clinopyroxene has been determined through the application of the stoichiometric formalism of Reference [38].

According to the two-feldspar thermometer (error ±30 °C) of Reference [59], the crystallization of plagioclase and alkali feldspar proceed in a temperature interval (~870–1006 °C) lower than that measured for clinopyroxene (Figure 9a). Importantly, the alkali feldspar-based hygrometer (error ±0.7 wt. % H_2O) of Reference [20] confirms that the degassing path of the sill magma is comprised between ~2.2 and ~0.3 wt. % H_2O (Figure 9a). Using these data and following the

same approach adopted by Reference [74], we have constrained the degassing-induced undercooling controlling the sill solidification. H_2O loss expands the liquidus surface of the melt and this effect can be parameterized through the polynomial function: $\Delta T = 40.4 \times H_2O - 2.9 \times H_2O^2 + 0.77 \times H_2O^3$ (see Reference [91] for further details). The use of this expression indicates that the degree of undercooling decreases from ~82 to ~14 °C upon progressive magma decompression and H_2O exsolution (Figure 9b), in agreement with data derived in a laboratory by Reference [74] and measured for a suite of natural Etnean products by Reference [75].

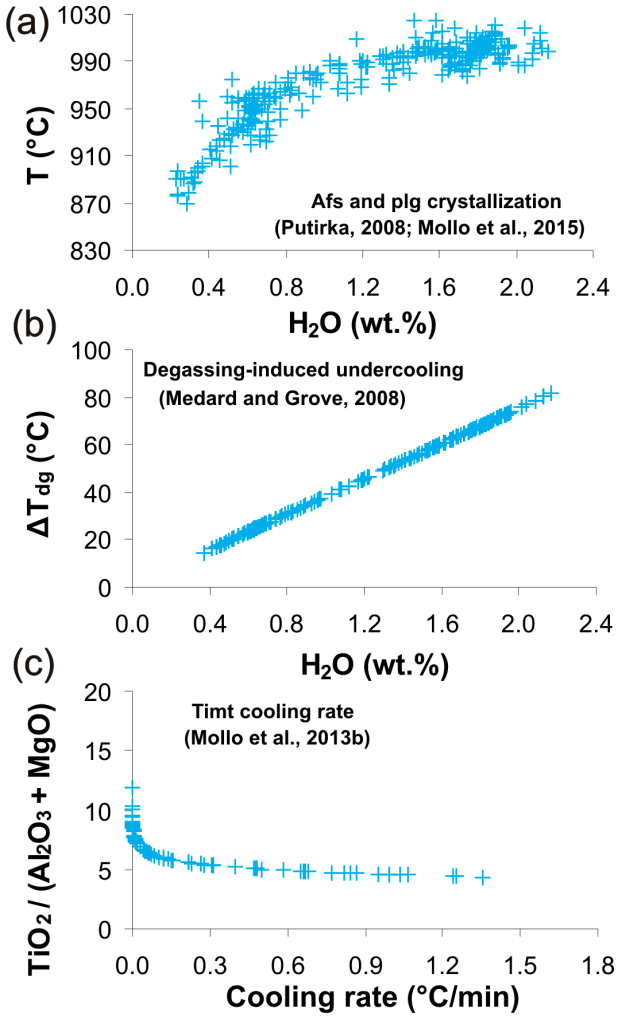

Figure 9. Temperatures (**a**) and melt-H_2O contents (**b**) in equilibrium with plagioclase and alkali feldspar have been estimated through the two-feldspar thermometer (error ±30 °C) of Reference [59] and thet alkali feldspar-based hygrometer (error ±0.7 wt. % H_2O) of Reference [20]. The degassing path and cooling rate of the sill magma (**c**) are predicted by the experimentally-derived equations of Reference [91] and Reference [37].

The plumbing system at Mt. Etna is governed by frequent inputs from mantle depths of primitive, volatile-rich magmas into shallower crustal reservoirs [9,13,18]. This continuous magma supply involves different magma batches that retain subtle differences in their *P*-*T* paths of ascent, with important repercussions for the role played by magma degassing on the crystallization and equilibration of different Etnean minerals [17]. For example, at P > 400 MPa and T > 1150 °C, the primitive and deep-seated Etnean magmas migrate very slowly towards the surface [17], because most of the volatiles are retained into the abundant melt phase. Due to (1) slow ascent rates at depth, (2) high H_2O contents and (3) low degrees of crystallization, the primitive magmas tend to

preserve their original basaltic to trachybasaltic compositions. Fractional crystallization modeling [18], thermodynamic calculations [13] and phase equilibria experiments [61] have illustrated that the segregation of 10–20% of phenocrysts at depth is the maximum admissible value to explain the persistent eruption of mafic alkaline products. In this context, thermodynamic data reported by Reference [20] indicate that primitive olivine and clinopyroxene phenocrysts equilibrate with magmas (58–68 Mg#) residing at high pressures and temperatures. In contrast, at shallower crustal levels, Etnean magmas are more differentiated (47–57 Mg#), because they undergo strong degassing and crystallization [16,22–25], especially during transit through the conduit to the surface [2,85,86]. For example, the continuous change in oxygen fugacity (Figure 7) is a proxy for the abundant degassing phenomena where H_2O-saturated magmas become more oxidized with increasing H_2O in excess [92,93]. Additionally, degassing magmas undergo significant hydrogen loss at subaerial conditions [73,94] or exposure to atmospheric oxygen [88,95]. Melt inclusion data indicate that volatile-rich magmas at Mt. Etna are rapidly decompressed from 400 to 100 MPa, experiencing extensive CO_2 loss, but still retaining a relatively high H_2O content [2,85,86]. Similarly, S (~0.3 wt. %), Cl (~0.3 wt. %), and F (~0.15 wt. %) start to exsolve only at low pressures of $\leq$140 MPa, <100 MPa, and $\leq$10 MPa. Degassing-driven crystallization controls the final crystal growth when most of the H_2O dissolved in the melt is rapidly exsolved [13], in concert with the upward acceleration of magma in the shallower parts of the plumbing system [17,75,84]. Under such circumstances, the near-equilibrium crystal growth at depth shifts towards a rapid (i.e., disequilibrium) crystal growth regime at syn-eruptive conditions. This is particularly evident for titanomagnetite microphenocrysts from the sill samples, recording kinetic effects caused by magma undercooling (Figure 6f). Under such circumstances, Ti is less favorably accommodated into the titanomagnetite crystal lattice, whereas Al and Mg are incorporated at non-equilibrium proportions. Through these Ti–Al–Mg cation substitutions, Reference [37] proposed a geospeedometer to estimate the cooling rate of the Etnean eruptions, providing a time-dependent temperature change up to 1.3 °C/min for the sill magma (Figure 9c). The complementary experimental data of Reference [83], Reference [74] and Reference [61] point out that most of the plagioclase and titanomagnetite microphenocryst contents (30–40%) in Etnean products form under cooling rates and ascent times of several hours. Travel times in the range of ~2–23 h are calculated by dividing the thermal path of the sill magma (Figure 9a) by the variable cooling rate (Figure 9c). Assuming an initial crystallization pressure of 200 MPa (Figure 8a) and a lithostatic pressure gradient of ~0.3 MPa/m [96], the travel times of the sill magma translate to ascent velocities of 0.07–0.78 m/s. Importantly, these estimates are consistent with the range of 0.01–0.63 m/s estimated for several eruptions at Mt. Etna [15,75,97], and documented for the eruptive activity of other open-conduit degassing volcanoes around the world [98–101].

4.3. Modeling the Geochemical Evolution of Magma

Microprobe data indicate that clinopyroxene and plagioclase phenocrysts from the sill samples are normally zoned with core-to-rim compositions varying from 0.84 to 0.76 mol. % DiHd and 0.67 to 0.56 mol. % An, respectively (Figure 2a,b). Coherently with major oxide analyses, REE concentrations in the crystals progressively increase, responding to cation incorporation mechanisms that were the subject of a great number of studies from literature (see references below). Adopting La and Yb as a proxy for LREE and HREE changes, respectively, Figure 10a shows that their concentrations in clinopyroxene increase with increasing ^{T}Al [102–111]. This positive correlation reflects an increased ease of locally balancing the excess charge at the M2 site as the number of surrounding tetrahedral Al atoms increases [66,112–118]. Since clinopyroxene can accommodate REE by adjusting its Al/Si ratio [45,66], the entry of REE into the M2 octahedral site is facilitated as the average charge on this site increases according to cation exchanges in which ^{M1}(Al, Fe^{3+}) substitute for ^{M2}(Mg, Fe^{2+}) coupled with replacement of ^{T}Al with Si [43,119]. This implies that the probability of achieving charge-neutral local configurations increases by increasing the CaTs in clinopyroxene at the expense of Di component [68,112,120]. For the case of plagioclase, REE enters

the M site by a charge balance mechanism where Na replaces Ca [121]. The substitution REE + Na → 2Ca in plagioclase occurs concurrently with the major cation substitution Ca + Al → Na + Si [122]. As a consequence, Figure 10b shows that the concentration of REE decreases with the increase of An, also responding to the smaller size of the anorthite octahedral site relative to that of albite [121,123–130]. Noteworthy, the dependence of REE on An incorporates also some important cross correlation effects related to the thermal path of the system (i.e., more calcic plagioclases equilibrate at a higher temperature [121,124,127,130]).

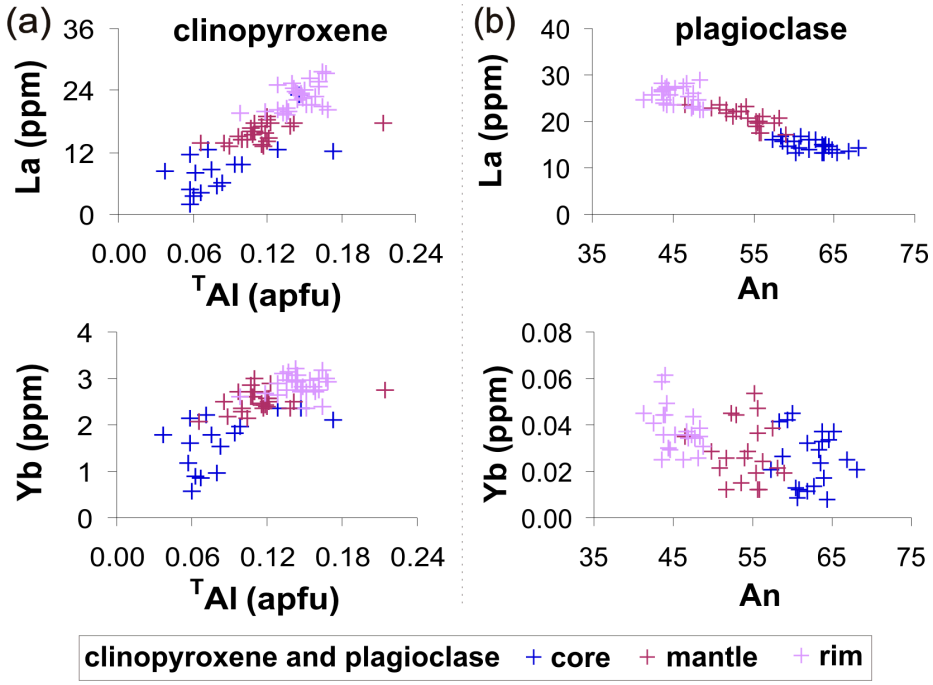

Figure 10. Geochemical evolution of La and Yb concentrations in phenocrysts plotted versus ^{T}Al in clinopyroxene (**a**) and An in plagioclase (**b**).

As anticipated from the preceding discussion, during magma evolution and crystal growth, the REE partition coefficients are not constant (cf. [66,131,132]), but rather change as a function of the physicochemical conditions of the system (Figures 8 and 9), dictating the final compositions of the zoned clinopyroxenes and plagioclases (Figure 10). In this view, the partitioning behavior of La (D_{La}) and Yb (D_{Yb}) has been modeled through the application of the lattice strain equations of Reference [62] and Reference [130] specific to clinopyroxene and plagioclase, respectively. The first model incorporates the effects of *P-T* [132], melt-H_2O content [126] and the electrostatic work involved in dissipating any local charge imbalance [66]. Crystal fractionation does not take place in one single and isolated magma batch, but rather occurs by multiple magma recharge events along with the entire vertically-developed plumbing system. The melt differentiation is extremely low and buffered to the almost constant composition of a trachybasalt [62]. This aspect is, however, deconvoluted in D_{La} and D_{Yb} modeling by considering the control of melt phase on trace element partitioning using the NBO/T parameter, referring to the number of non-bridging oxygens per tetrahedral cations in the melt [62]. The second model consists of a parameterized lattice strain equation accounting for the effects of pressure, temperature, and Ca content in plagioclase, being the only dominant factors controlling the partitioning of trace elements between plagioclase and melt [130]. D_{La} and D_{Yb} from calculations are plotted versus the amounts of CaTs (Figure 11a) and An (Figure 11b) in clinopyroxene and plagioclase, respectively (Table S6 submitted as Supplementary Materials). The partition coefficients monotonically increase along with the geochemical evolution of minerals, evidencing the variable REE affinity for the CaTs-rich clinopyroxene and An-poor plagioclase compositions formed during magma crystallization. D_{La} and

D_{Yb} increase about twice during clinopyroxene and plagioclase growth, pointing out the importance of considering the change of trace element partitioning for a better understanding of magmatic differentiation processes. To quantitatively assess the role played by clinopyroxene and plagioclase fractionation on the trace element pattern of the sill magma, the whole ranges of D_{La} and D_{Yb} values calculated through the lattice strain equations have been used as input data for the Rayleigh fractional crystallization (FC) equation: $C_l = C_0 F^{(D-1)}$ where C_l is the trace element concentration in the residual melt, C_0 is the concentration in the starting composition, and F is the fraction of melt remaining. The extent of clinopyroxene ($\leq$41%) and plagioclase ($\leq$12%) fractionation was varied so that the resulting values of C_l reproduced the bulk trace element concentrations of natural products (cf. [133]). It is worth noting that the total amount of solid segregated matches very well with the high phenocryst content (~40%) of products from Valle del Bove, and mass balance and thermodynamic calculations constraining the transition from trachybasalts to trachyandesites [16,22,24,25]. Stepwise calculations were performed assuming early fractionation of clinopyroxene at depth followed by dominant feldspar cosaturation during magma ascent and volatile exsolution (cf. [133]). To perform these calculations, bulk rock trace element compositions of eruptions at Valle del Bove have been recovered from the GEOROC database. Inspection of the analytical dataset shows that, in contrast to major oxide data, only a restricted number of bulk rock trace element compositions have been provided by authors [22,23,25,26,58] and that analytical data are generally incomplete. Despite the concentrations of REE are frequently reported, there is a poor correspondence among the different works, because several elements are randomly missing. Bearing in mind this critical restriction, it is generally verified that LREE and HREE increase (up to ~118 ppm La and ~3 ppm Yb, respectively) with increasing SiO_2 (~47–61 wt. %) of the magma. The most primitive basaltic samples contain ~30 ppm La and ~1 ppm Yb (data from Reference [22]), providing fairly good constraints for the C_0 starting composition of FC modeling. Results from calculations are plotted in Figure 12, together with the natural compositions of eruptions at Valle del Bove. The primary ^{cpx}FC vector is consistent with the development of a fractional crystallization-dominated environment at depth controlled prevalently by the early formation of clinopyroxene at a relatively high temperature [16,17,25]. The non-linear trajectory of the vector testifies to Ce and Y incorporation in the crystal lattice at different proportions and provides an explanation for the incipient variability of the natural dataset. On the other hand, the crystallization of feldspar is restricted to very shallow conditions upon the effect of degassing and cooling [11,13,19,61,74,83]. Indeed, clinopyroxene phenocryst rims record a more evident europium anomaly (Figure 4a), suggesting prevalent plagioclase formation at the final stage of clinopyroxene growth. The complementary ^{plg}FC1, ^{plg}FC2 and ^{plg}FC3 vectors account for low degrees of feldspar fractionation after variable amounts of clinopyroxene segregation (Figure 12). The linear trends depicted by the vectors are caused by the highly incompatible behavior of La and Yb in plagioclase. Overall, the modeled evolutionary trajectories match very well with the bulk rock compositions of the sill and natural magmas at Valle del Bove (Figure 12). The early fractionation of clinopyroxene at depth controls the original REE signature of the basaltic products [16,25], whereas subsequent degassing at low pressure conditions enlarges the stability field of plagioclase via H_2O exsolution [23,83,85], thus driving trace element enrichments in basaltic trachyandesites and trachyandesites (Figure 12).

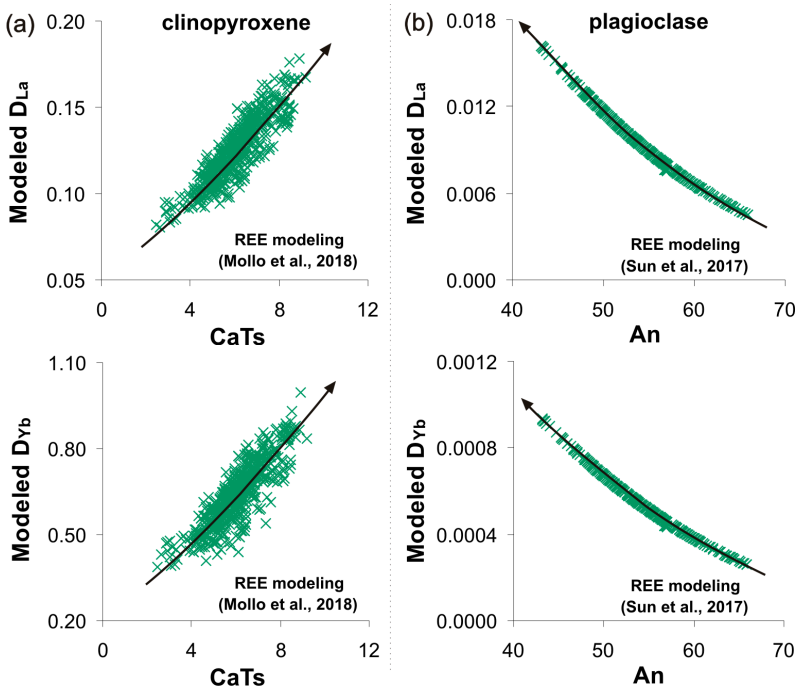

Figure 11. The partition coefficients of La (D_{La}) and Yb (D_{Yb}) have been modeled as a function of clinopyroxene (**a**) and plagioclase (**b**) geochemical evolution along with the decompression and cooling path of the sill magma. CaTs and An refer to Ca-Tschermak and An components. The partitioning data have been modeled through the lattice strain equations of Reference [62] and Reference [130] specific to clinopyroxene and plagioclase, respectively. See Table S6 submitted as Supplementary Materials.

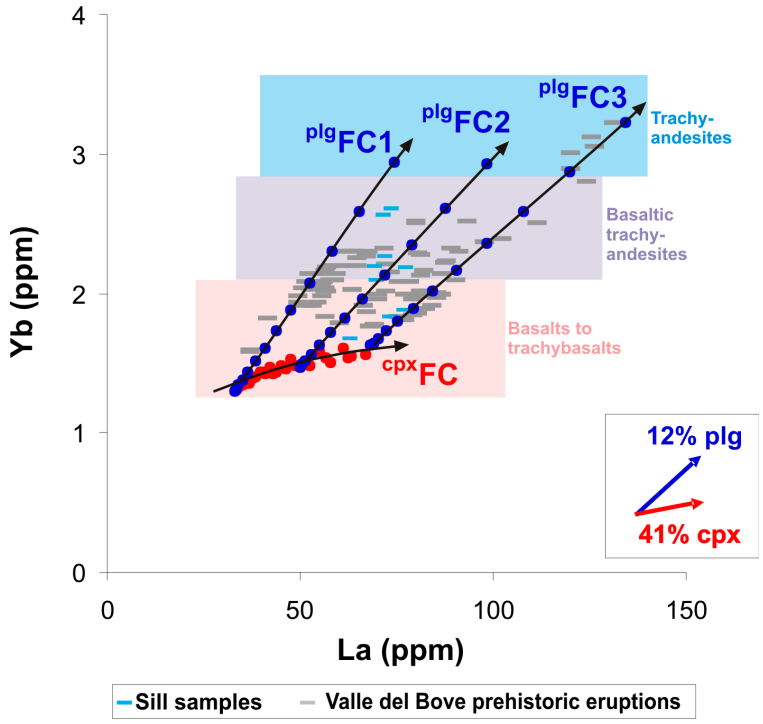

Figure 12. La vs. Yb diagram showing the geochemical evolution of the magma sill in the framework of prehistoric eruptions at Valle del Bove. These data have been modeled through the Rayleigh fractional crystallization equation. At the beginning of the modeling, the early fractionation of clinopyroxene at depth has been considered. Stepwise calculations were performed changing D_{La} and D_{Yb} at each step of fractionation as a function of the geochemical evolution of clinopyroxene.

Modeled La and Yb concentrations were used to draw the ^{cpx}FC vector. Fractional crystallization calculations were further developed accounting for the segregation of plagioclase during magma decompression and degassing at shallow crustal conditions. Modeling results are aligned along different ^{plg}FC vectors.

5. Conclusions

This study presents major and trace element analyses of bulk rocks and minerals from the central part of an Etnean sill outcropping at Valle del Bove depression. Modeling data derived by the application of *P*-*T*-H_2O-lattice strain equations leads to the following conclusions:

1. The overall decompression and cooling path of magma is constrained by pressure and temperature changes of 0.1–200 MPa and 1050–870 °C, respectively;
2. The ascent of magma is accompanied by H_2O exsolution up to ~2.2 wt. %, causing magma acceleration during ascent to the surface and degassing-induced undercooling phenomena;
3. The early formation of clinopyroxene at depth is the main controlling factor for the REE signature of primitive basalts at Valle del Bove;
4. In contrast, late degassing at low pressure conditions favors plagioclase crystallization and trace element enrichments in the more evolved trachyandesitic eruptions.

Supplementary Materials: The following are available online at http://www.mdpi.com/2075-163X/9/2/126/s1, Table S1: Clinopyroxene compositions; Table S2: Feldspar (plagioclase and alkali feldspar) compositions; Table S3: Titanomagnetite compositions; Table S4: Rare earth element (REE) concentrations of clinopyroxene and plagioclase; Table S5: Major and trace element concentrations of bulk rocks; Table S6: Modeled partition coefficients for La and Yb.

Author Contributions: Conceptualization, M.N., F.D.S., S.M.; Formal Analysis, M.N. and V.T.; Investigation, M.N., F.D.S., S.M.; Data Curation, M.N., F.D.S., S.M., P.S., V.T., B.E., O.B., C.F.; Writing—Original Draft Preparation, M.N., F.D.S., S.M., P.S., V.T., B.E., O.B., C.F.; Writing—Review and Editing, M.N., F.D.S., S.M., P.S., V.T., B.E., O.B., C.F.; Visualization, M.N., F.D.S., S.M., P.S., V.T., B.E., O.B., C.F.; Funding Acquisition, M.N., F.D.S., S.M., P.S., V.T., B.E., O.B., C.F.

Funding: This research received no external funding.

Acknowledgments: Thanks go to Marcel Guillong for his support with laser ablation analyses.

Conflicts of Interest: The authors declare no conflict of interest.

References

1. Branca, S.; Coltelli, M.; De Beni, E.; Wijbrans, J. Geological evolution of Mount Etna volcano (Italy) from earliest products until the first central volcanism (between 500 and 100 ka ago) inferred from geochronological and stratigraphic data. *Int. J. Earth Sci.* **2008**, *97*, 135–152. [CrossRef]
2. Collins, S.J.; Pyle, D.M.; Maclennan, J. Melt inclusions track pre-eruption storage and dehydration of magmas at Etna. *Geology* **2009**, *37*, 571–574. [CrossRef]
3. Ferlito, C.; Coltorti, M.; Lanzafame, G.; Giacomoni, P.P. The volatile flushing triggers eruptions at open conduit volcanoes: Evidence from Mount Etna volcano (Italy). *Lithos* **2014**, *184–187*, 447–455. [CrossRef]
4. Ferlito, C. Mount Etna volcano (Italy). Just a giant hot spring! *Earth-Sci. Rev.* **2017**, *177*, 14–23. [CrossRef]
5. Mollo, S.; Vetere, F.; Beherens, H.; Tecchiato, V.; Langone, A.; Scarlato, P.; Perugini, D. The effect of degassing and volatile exsolution on the composition of a trachybasaltic melt decompressed at slow and fast rates. *Per. Min.* **2017**, *86*, 185–197. [CrossRef]
6. Perinelli, C.; Mollo, S.; Gaeta, M.; De Cristofaro, S.P.; Palladino, D.M.; Scarlato, P. Impulsive Supply of Volatile-Rich Magmas in the Shallow Plumbing System of Mt. Etna Volcano. *Minerals* **2018**, *8*, 482. [CrossRef]
7. Kamenetsky, V.S.; Pompilio, M.; Métrich, N.; Sobolev, A.V.; Kuzmin, D.V.; Thomas, R. Arrival of extremely volatile-rich high-Mg magmas changes explosivity of Mount Etna. *Geology* **2007**, *35*, 255–258. [CrossRef]
8. Ferlito, C.; Coltorti, M.; Cristofolini, R.; Giacomoni, P.P. The contemporaneous emission of low-K and high-K trachybasalts and the role of the NE Rift during the 2002 eruptive event, Mt. Etna, Italy. *Bull. Volcanol.* **2009**, *71*, 575–587. [CrossRef]

9. Ferlito, C.; Viccaro, M.; Cristofolini, R. Volatile-induced magma differentiation in the plumbing system of Mt. Etna volcano (Italy): Evidence from glass in tephra of the 2001 eruption. *Bull. Volcanol.* **2008**, *70*, 455–473. [CrossRef]
10. Ferlito, C.; Lanzafame, G. The role of supercritical fluids in the potassium enrichment of magmas at Mount Etna volcano (Italy). *Lithos* **2010**, *119*, 642–650. [CrossRef]
11. Giacomoni, P.P.; Ferlito, C.; Coltorti, M.; Bonadiman, C.; Lanzafame, G. Plagioclase as archive of magma ascent dynamics on "open conduit" volcanoes: The 2001-2006 eruptive period at Mt. Etna. *Earth-Sci. Rev.* **2014**, *138*, 371–393. [CrossRef]
12. Kahl, M.; Chakraborty, S.; Pompilio, M.; Costa, F. Constraints on the nature and evolution of the magma plumbing system of Mt. Etna volcano (1991-2008) from a combined thermodynamic and kinetic modelling of the compositional record of minerals. *J. Petrol.* **2015**, *56*, 2025–2068. [CrossRef]
13. Mollo, S.; Giacomoni, P.P.; Andronico, D.; Scarlato, P. Clinopyroxene and titanomagnetite cation redistributions at Mt. Etna volcano (Sicily, Italy): Footprints of the final solidification history of lava fountains and lava flows. *Chem. Geol.* **2015**, *406*, 45–54. [CrossRef]
14. Giacomoni, P.P.; Coltorti, M.; Mollo, S.; Ferlito, C.; Braiato, M.; Scarlato, P. The 2011–2012 paroxysmal eruptions at Mt. Etna volcano: Insights on the vertically zoned plumbing system. *J. Volcanol. Geotherm. Res.* **2018**, *349*, 370–391. [CrossRef]
15. Ubide, T.; Kamber, B.S. Volcanic crystals as time capsules of eruption history. *Nat. Commun.* **2018**, *9*, 1–12. [CrossRef] [PubMed]
16. Armienti, P.; Tonarini, S.; Innocenzi, F.; D'Orazio, M. Mount Etna pyroxene as tracer of petrogenetic processes and Dynamics of the Feeding System. *Geol. Soc. Am.* **2007**, *418*, 265–276. [CrossRef]
17. Armienti, P.; Perinelli, C.; Putirka, K.D. A new model to estimate deep-level magma ascent rates, with applications to Mt. Etna (Sicily, Italy). *J. Petrol.* **2013**, *54*, 795–813. [CrossRef]
18. Corsaro, R.A.; Di Renzo, V.; Distefano, S.; Miraglia, L.; Civetta, L. Relationship between petrologic processes in the plumbing system of Mt. Etna and the dynamics of the eastern flank from 1995 to 2005. *J. Volcanol. Geotherm. Res.* **2013**, *251*, 75–89. [CrossRef]
19. Lanzafame, G.; Mollo, S.; Iezzi, G.; Ferlito, C.; Ventura, G. Unraveling the solidification path of a pahoehoe "cicirara" lava from Mount Etna volcano. *Bull. Volcanol.* **2013**, *75*, 1–16. [CrossRef]
20. Mollo, S.; Giacomoni, P.P.; Coltorti, M.; Ferlito, C.; Iezzi, G.; Scarlato, P. Reconstruction of magmatic variables governing recent Etnean eruptions: Constraints from mineral chemistry and P–T–fO_2–H_2O modeling. *Lithos* **2015**, *215*, 311–320. [CrossRef]
21. Corsaro, R.A.; Civetta, L.; Di Renzo, V.; Miraglia, L. Petrology of lavas from the 2004-2005 flank eruption of Mt. Etna, Italy: Inferences on the dynamics of magma in the shallow plumbing system. *Bull. Volcanol.* **2009**, *71*, 781–793. [CrossRef]
22. D'Orazio, M.; Tonarini, S.; Innocenti, F.; Pompilio, M. The northern Valle del Bove volcanic succession (Mt. Etna, Sicily): Petrography, geochemistry and Sr-Nd isotope data. *Acta Vulcanol.* **1997**, *9*, 69–79.
23. Tanguy, J.; Condomines, M.; Kieffer, G.; Sevier, E.L.; Tanguy, J.; Condomines, M.; Kieffer, G. Evolution of the Mount Etna magma: Constraints on the present feeding system and eruptive mechanism. *J. Volcanol. Geotherm. Res.* **1997**, *75*, 221–250. [CrossRef]
24. Corsaro, R.A.; Cristofolini, R.; Patanè, L. The 1669 eruption at Mount Etna: Chronology, petrology and geochemistry, with inferences on the magma sources and ascent mechanisms. *Bull Volcanol* **1996**, *58*, 348–358. [CrossRef]
25. Armienti, P.; Tonarini, S.; D'Orazio, M.; Innocenti, F. Genesis and evolution of Mt. Etna alkaline lavas: Petrological and Sr-Nd-B isotope constraints. *Period. Mineral.* **2004**, *73*, 29–52.
26. Ferlito, C.; Nicotra, E. The dyke swarm of Mount Calanna (Etna, Italy): An example of the uppermost portion of a volcanic plumbing system. *Bull. Volcanol.* **2010**, *72*, 1191–1207. [CrossRef]
27. Patanè, D.; Barberi, G.; Cocina, O.; De Gori, P.; Chiarabba, C. Time-resolved seismic tomography detects magma intrusions at mount etna. *Science* **2006**, *313*, 821–823. [CrossRef] [PubMed]
28. Palano, M.; Puglisi, G.; Gresta, S. Ground deformation patterns at Mt. Etna from 1993 to 2000 from joint use of InSAR and GPS techniques. *J. Volcanol. Geotherm. Res.* **2008**, *169*, 99–120. [CrossRef]
29. Bonforte, A.; Bonaccorso, A.; Guglielmino, F.; Palano, M.; Puglisi, G. Feeding system and magma storage beneath Mt. Etna as revealed by recent inflation/deflation cycles. *JGR Solid Earth* **2008**, *113*, 1–13. [CrossRef]

30. Bonaccorso, A.; Bonforte, A.; Calvari, S.; Del Negro, C.; Di Grazia, G.; Ganci, G.; Neri, M.; Vicari, A.; Boschi, E. The initial phases of the 2008-2009 Mount Etna eruption: A multidisciplinary approach for hazard assessment. *J. Geophys. Res. Solid Earth* **2011**, *116*, 1–19. [CrossRef]
31. Guillong, M.; Meier, D.L.; Allan, M.M.; Heinrich, C.A.; Yardley, B.W. Appendix A6: SILLS: A MATLAB-based program for the reduction of laser ablation ICP-MS data of homogeneous materials and inclusions. In *Laser Ablation–ICP–MS in the Earth Sciences: Current Practices and Outstanding Issues*; Sylvester, P., Ed.; Mineralogical Association of Canada Short Course Series Volume 40; Mineralogical Association of Canada: Québec, QC, Canada, 2008; pp. 328–333.
32. Corsaro, R.A.; Cristofolini, R. Nuovi dati petrochimici ed isotopici sulla successione del Mongibello Recente. *Boll. Acc. Gioenia. Sci. Nat.* **1993**, *341*, 185–225.
33. Armienti, P.; Barberi, F.; Innocenti, F. A model of the Phlegraean Fields magma chamber in the last 10,500 years. *Bull. Volcanol.* **1984**, *47*, 349–358. [CrossRef]
34. Murphy, M.D.; Sparks, R.S.J.; Barclay, J.; Carroll, M.R.; Brewer, T.S. Remobilization of andesite magma by intrusion of mafic magma at the Soufriere Hills Volcano, Montserrat, West Indies. *J. Petrol.* **2000**, *41*, 21–42. [CrossRef]
35. Mollo, S.; Putirka, K.; Misiti, V.; Soligo, M.; Scarlato, P. A new test for equilibrium based on clinopyroxene-melt pairs: clues on the solidification temperatures of Etnean alkaline melts at post-eruptive conditions. *Chem. Geol.* **2013**, *352*, 92–100. [CrossRef]
36. Mollo, S.; Del, P.; Ventura, G.; Iezzi, G.; Scarlato, P. Dependence of clinopyroxene composition on cooling rate in basaltic magmas: Implications for thermobarometry. *Lithos* **2010**, *118*, 302–312. [CrossRef]
37. Mollo, S.; Blundy, J.D.; Scarlato, P.; Iezzi, G.; Langone, A. The partitioning of trace elements between clinopyroxene and trachybasaltic melt during rapid cooling and crystal growth. *Contrib. Mineral. Petrol.* **2013**, *166*, 1633–1654. [CrossRef]
38. Lindsley, D.H. Pyroxene thermometry. *Am Mineral.* **1983**, *68*, 477–493.
39. Putirka, K.D.; Johnson, M.; Kinzler, R.; Longhi, J.; Walker, D. Thermobarometry of mafic igneous rocks based on clinopyroxene-liquid equilibria, 0–30 kbar. *Contrib. Mineral. Petrol.* **1996**, *123*, 92–108. [CrossRef]
40. Morimoto, N.; Fabries, J.; Ferguson, A.K.; Ginzburg, I.V.; Ross, M.; Seifert, F.A.; Zussman, J.; Aoki, K.; Gottardi, G. Nomenclature of pyroxenes. *Mineral. Mag.* **1988**, *52*, 535–550. [CrossRef]
41. Muñoz, M.; Sagredo, J. Clinopyroxenes as geobarometric indicators in mafic and ultramafic rocks from Canary Islands. *Contrib. Mineral. Petrol.* **1974**, *44*, 139–147. [CrossRef]
42. Mollo, S.; Lanzafame, G.; Masotta, M.; Iezzi, G.; Ferlito, C.; Scarlato, P. Cooling history of a dike as revealed by mineral chemistry: a case study from Mt. Etna volcano. *Chem. Geol.* **2011**, *288*, 39–52. [CrossRef]
43. Mollo, S.; Blundy, J.D.; Giacomoni, P.P.; Nazzari, M.; Scarlato, P.; Coltorti, M.; Langone, A.; Andronico, D. Clinopyroxene-melt element partitioning during interaction between trachybasaltic magma and siliceous crust: clues from quartzite enclaves at Mt. Etna volcano. *Lithos* **2017**, *284–285*, 447–461. [CrossRef]
44. Sun, S.-S.; McDonough, W.F. Chemical and isotopic systematics of oceanic basalts: Implications for mantle composition and processes. In *Magmatism in the Ocean Basins*; Saunders, A.D., Norry, M.J., Eds.; Geological Society, London, Special Publication; Geological Society of London: London, UK, 1989; pp. 13–345.
45. Scarlato, P.; Mollo, S.; Blundy, J.D.; Iezzi, G.; Tiepolo, M. The role of natural solidification paths on REE partitioning between clinopyroxene and melt. *Bull. Volcanol.* **2014**, *76*, 1–4. [CrossRef]
46. Giacomoni, P.P.; Coltorti, M.; Bryce, J.G.; Fahnestock, M.F.; Guitreau, M. Mt. Etna plumbing system revealed by combined textural, compositional, and thermobarometric studies in clinopyroxenes. *Contrib. Mineral. Petrol.* **2016**, *171*, 1–15. [CrossRef]
47. Smith, C.B. Pb, Sr and Nd isotopic evidence for sources of Southern African Cretaceous kimberlites. *Nature* **1983**, *30*, 51–54. [CrossRef]
48. Smith, J.V.; Brown, W.L. *Feldspar Minerals*; Volume I; Springer-Verlag: Berlin/Heidelberg, Germany, 1988.
49. Loomis, T.P. An investigation of disequilibrium growth processes of plagioclase in the system anorthite-albite-water by methods of numerical simulation. *Contrib. Mineral. Petrol.* **1981**, *76*, 196–205. [CrossRef]
50. Loomis, T.P.; Welber, P.W. Crystallization processes in the Rocky Hill Sanodiorite pluton, California: An interpretation based on compositional zoning of plagioclase. *Contrib. Mineral. Petrol.* **1982**, *81*, 230–239. [CrossRef]

51. Tegner, C. Iron in plagioclase as a monitor of the differentiation of the Skaergaard intrusion. *Contrib. Mineral. Petrol.* **1997**, *128*, 45–51. [CrossRef]
52. Pietranik, A.; Koepke, J.; Puziewicz, J. Crystallization and resorption in plutonic plagioclase: Implications on the evolution of granodiorite magma (Gesiniec granodiorite, Strzelin Crystalline Massif, SW Poland). *Lithos* **2006**, *86*, 260–280. [CrossRef]
53. Mollo, S.; Putirka, K.; Iezzi, G.; Del Gaudio, P.; Scarlato, P. Plagioclase–melt (dis)equilibrium due to cooling dynamics: Implications for thermometry, barometry and hygrometry. *Lithos* **2011**, *125*, 221–235. [CrossRef]
54. Viccaro, M.; Ferlito, C.; Cortesogno, L.; Cristofolini, R.; Gaggero, L. Magma mixing during the 2001 event at Mount Etna (Italy): Effects on the eruptive dynamics. *J. Volcanol. Geotherm. Res.* **2006**, *149*, 139–159. [CrossRef]
55. Stormer, J.C. The effects of recalculation on estimates of temperature and oxygen fugacity from analyses of multicomponent iron-titanium oxides. *Am. Mineral.* **1983**, *68*, 586–594.
56. Zhou, W.; Van Der Voo, R.; Peacor, D.R.; Zhang, Y. Variable Ti-content and grain size of titanomagnetite as a function of cooling rate in very young MORB. *Earth Planet. Sci. Lett.* **2000**, *179*, 9–20. [CrossRef]
57. Le Bas, M.J.; Le Maitre, R.W.; Streckeisen, A.; Zanettin, B. A chemical classification of volcanic rocks on the total alkali-silica diagram. *J. Petrol.* **1986**, *27*, 745–750. [CrossRef]
58. D'Orazio, M.; Armienti, P.; Cerretini, S. Petrology Phenocryst/matrix trace-element partition coefficients for hawaiite-trachyte lavas from the Ellittico volcanic sequence (Mt. Etna, Sicily, Italy). *Mineral. Petrol.* **1998**, *64*, 65–88. [CrossRef]
59. Putirka, K.D. Thermometers and Barometers for Volcanic Systems. *Rev. Mineral. Geochem.* **2008**, *69*, 61–120. [CrossRef]
60. Lanzafame, G.; Iezzi, G.; Mancini, L.; Lezzi, F.; Mollo, S.; Ferlito, C. Solidification and Turbulence (Non-laminar) during Magma Ascent: Insights from 2D and 3D Analyses of Bubbles and Minerals in an Etnean Dyke. *J. Petrol.* **2017**, *58*, 1511–1533. [CrossRef]
61. Vetere, F.; Mollo, S.; Giacomoni, P.P.; Iezzi, G.; Coltorti, M.; Ferlito, C.; Holtz, F.; Perugini, D.; Scarlato, P. Experimental constraints on the origin of pahoehoe "cicirara" lavas at Mt. Etna Volcano (Sicily, Italy). *Bull. Volcanol.* **2015**, *77*. [CrossRef]
62. Mollo, S.; Blundy, J.D.; Scarlato, P.; De Cristofaro, S.P.; Tecchiato, V.; Di Stefano, F.; Vetere, F.; Holtz, F.; Bachmann, O. An integrated P-T-H_2O-lattice strain model to quantify the role of clinopyroxene fractionation on REE+Y and HFSE patterns of mafic alkaline magmas: Application to eruptions at Mt. Etna. *Earth-Sci. Rev.* **2018**, *185*, 32–56. [CrossRef]
63. Mollo, S.; Hammer, J.E. Dynamic crystallization in magmas. In *Mineral Reaction Kinetics: Microstructures, Textures, Chemical and Isotopic Signatures*; Heinrich, W., Abart, R., Eds.; Mineralogical Society: Chantilly, VA, USA, 2017; pp. 378–418.
64. Mollo, S.; Masotta, M. Optimizing pre-eruptive temperature estimates in thermally and chemically zoned magma chambers. *Chem. Geol.* **2014**, *368*, 97–103. [CrossRef]
65. Hill, E.; Blundy, J.D.; Wood, B.J. Clinopyroxene–melt trace element partitioning and the development of a predictive model for HFSE and Sc. *Contrib. Mineral. Petrol.* **2011**, *161*, 423–438. [CrossRef]
66. Wood, B.J.; Trigila, R. Experimental determination of aluminous clinopyroxene-melt partition coefficients for potassic liquids, with application to the evolution of the Roman province potassic magmas. *Chem. Geol.* **2001**, *172*, 213–223. [CrossRef]
67. Mollo, S.; Misiti, V.; Scarlato, P.; Soligo, M. The role of cooling rate in the origin of high temperature phases at the chilled margin of magmatic intrusions. *Chem. Geol.* **2012**, *322–323*, 28–46. [CrossRef]
68. Mollo, S.; Putirka, K.; Iezzi, G.; Scarlato, P. The control of cooling rate on titanomagnetite composition: implications for a geospeedometry model applicable to alkaline rocks from Mt. Etna volcano. *Contrib. Mineral. Petrol.* **2013**, *165*, 457–475. [CrossRef]
69. Putirka, K.D.; Mikaelian, H.; Ryerson, F.; Shaw, H. New clinopyroxene-liquid thermobarometers for mafic, evolved, and volatile-bearing lava compositions, with applications to lavas from Tibet and the Snake River Plain, Idaho. *Am. Mineral.* **2003**, *88*, 1542–1554. [CrossRef]
70. Namur, O.; Charlier, B.; Toplis, M.J.; Vander Auwera, J. Prediction of plagioclase-melt equilibria in anhydrous silicate melts at 1-atm. *Contrib. Mineral. Petrol.* **2012**, *163*, 133–150. [CrossRef]
71. Hamada, M.; Fujii, T. Experimental constraints on the effects of pressure and H_2O on the fractional crystallization of high-Mg island arc basalt. *Contrib. Mineral. Petrol.* **2008**, *155*, 767–790. [CrossRef]

72. Ushioda, M.; Takahashi, E.; Hamada, M.; Suzuki, T. Water content in arc basaltic magma in the Northeast Japan and Izu arcs: An estimate from Ca/Na partitioning between plagioclase and melt. *Earth Planets Space* **2014**, *66*, 127. [CrossRef]
73. Sisson, T.W.; Grove, T.L. Temperatures and H_2O contents of low-MgO high-alumina basalts. *Contrib. Mineral. Petrol.* **1993**, *113*, 167–184. [CrossRef]
74. Applegarth, L.J.; Tuffen, H.; James, M.R.; Pinkerton, H.; Cashman, K.V. Direct observations of degassing-induced crystallization in basalts. *Geology* **2013**, *41*, 243–246. [CrossRef]
75. Mollo, S.; Masotta, M.; Forni, F.; Bachmann, O.; Astis, D.; Moore, G.; Scarlato, P. A K-feldspar–liquid hygrometer specific to alkaline differentiated magmas. *Chem. Geol.* **2015**, *392*, 1–8. [CrossRef]
76. Ishibashi, H. Spinel-melt oxygen barometry; a method and application to Cenozoic alkali basaltic magmas from the Higashi-Matsuura District, NW Kyushu, Japan. *Geosci. Rep. Shizuoka Univ.* **2013**, *40*, 21–32.
77. Ariskin, A.A.; Nikolaev, G.S. An empirical model for the calculation of spinel-melt equilibria in mafic igneous systems at atmospheric pressure: 1. Chromian spinels. *Contrib. Mineral. Petrol.* **1996**, *123*, 282–292. [CrossRef]
78. Sack, R.O. Some constraints on the thermodynamic mixing properties of Fe–Mg orthopyroxenes and olivines. *Contrib. Mineral. Petrol.* **1980**, *71*, 257–269. [CrossRef]
79. Armienti, P.; Pareschi, M.T.; Innocenti, F.; Pompilio, M. Effects of magma storage and ascent on the kinetics of crystal growth—The case of the 1991-93 Mt. Etna eruption. *Contrib. Mineral. Petrol.* **1994**, *115*, 402–414. [CrossRef]
80. Lundgaard, K.L.; Tegner, C. Partitioning of ferric and ferrous iron between plagioclase and silicate melt. *Contrib. Mineral. Petrol.* **2004**, *147*, 470–483. [CrossRef]
81. Tanguy, J.C.; Clocchiatti, R. The Etnean Lavas, 1977-1983: Petrology and mineralogy. *Bull. Volcanol.* **1984**, *47*, 879–894. [CrossRef]
82. Dolfi, D.; Trigila, R. Clinopyroxene solid solutions and water in magmas: Results in the system phonolitic tephrite-H_2O. *Mineral. Mag.* **1983**, *47*, 347–351. [CrossRef]
83. Métrich, N.; Rutherford, M.J. Low pressure crystallization paths of H_2O-saturated basaltic-hawaiitic melts from Mt Etna: Implications for open-system degassing of basaltic volcanoes. *Geochim. Cosmochim. Acta* **1998**, *62*, 1195–1205. [CrossRef]
84. Perinelli, C.; Mollo, S.; Gaeta, M.; De Cristofaro, S.P.; Palladino, D.M.; Armienti, P.; Scarlato, P.; Putirka, K.D. An improved clinopyroxene-based hygrometer for Etnean magmas and implications for eruption triggering mechanisms. *Am. Mineral.* **2016**, *101*, 2774–2777. [CrossRef]
85. Métrich, N.; Allard, P.; Spilliaert, N.; Andronico, D.; Burton, M. 2001 flank eruption of the alkali- and volatile-rich primitive basalt responsible for Mount Etna's evolution in the last three decades. *Earth Planet. Sci. Lett.* **2004**, *228*, 1–17. [CrossRef]
86. Spilliaert, N.; Métrich, N.; Allard, P. S-Cl-F degassing pattern of water-rich alkali basalt: Modelling and relationship with eruption styles on Mount Etna volcano. *Earth Planet. Sci. Lett.* **2006**, *248*, 772–786. [CrossRef]
87. Witham, F.; Blundy, J.D.; Kohn, S.C.; Lesne, P.; Dixon, J.; Churakov, S.V.; Botcharnikov, R. SolEx: A model for mixed COHSCl-volatile solubilities and exsolved gas compositions in basalt. *Comp. Geosci.* **2012**, *45*, 87–97. [CrossRef]
88. Mollo, S.; Scarlato, P.; Lanzafame, G.; Ferlito, C. Deciphering lava flow posteruption differentiation processes by means of geochemical and isotopic variations: A case study from Mt. Etna volcano. *Lithos* **2013**, *162–163*, 115–127. [CrossRef]
89. Gardner, J.E.; Rutherford, M.; Carey, S.; Sigurdsson, H. Experimental constraints on pre-eruptive water contents and changing magma storage prior to explosive eruptions of Mount St. Helens volcano. *Bull. Volcanol.* **1995**, *57*, 1–17. [CrossRef]
90. Frey, H.M.; Lange, R.A. Phenocryst complexity in andesites and dacites from the Tequila volcanic field, Mexico: Resolving the effects of degassing vs. magma mixing. *Contrib. Mineral. Petrol.* **2011**, *162*, 415–445. [CrossRef]
91. Médard, E.; Grove, T.L. The effect of H_2O on the olivine liquidus of basaltic melts: Experiments and thermodynamic models. *Contrib. Mineral. Petrol.* **2008**, *155*, 417–432. [CrossRef]
92. Del Bello, E.; Mollo, S.; Scarlato, P.; von Quadt, A.; Forni, F.; Bachmann, O. New petrological constraints on the last eruptive phase of the Sabatini Volcanic District (central Italy): Clues from mineralogy, geochemistry, and Sr-Nd isotopes. *Lithos* **2014**, *205*, 28–38. [CrossRef]

93. Moore, G.; Righter, K.; Carmichael, I.S.E. The effect of dissolved water on the oxidation state of iron in natural silicate liquids. *Contrib. Mineral. Petrol.* **1995**, *120*, 170–179. [CrossRef]
94. Mathez, E.A. Influence of degassing on oxidation states of basaltic magmas. *Nature* **1984**, *310*, 371–375. [CrossRef]
95. Furukawa, H.; Ko, N.; Go, Y.B.; Aratani, N.; Choi, S.B.; Choi, E.; Özgür Yazaydin, A.; Snurr, R.Q.; O'Keeffe, M.; Kim, J.; et al. Ultrahigh porosity in metal–organic frameworks. *Science* **2010**, *329*, 424–428. [CrossRef] [PubMed]
96. Corsaro, R.A.; Pompilio, M. Magma dynamics in the shallow plumbing system of Mt. Etna as recorded by compositional variations in the volcanics of recent summit activity (1995–1999). *J. Volc. Geotherm. Res.* **2004**, *137*, 55–71. [CrossRef]
97. Aloisi, M.; Bonaccorso, A.; Gambino, S. Imaging composite dike propagation (Etna, 2002 case). *J. Geophys. Res. Solid Earth* **2006**, *111*, 1–13. [CrossRef]
98. Rutherford, M.J.; Hill, P.M. Magma ascent rates from amphibole breakdown: experiments and the 1980–1986 Mount St. Helens eruptions. *J. Geophys. Res. Solid Earth* **1993**, *98*, 19667–19685. [CrossRef]
99. Rutherford, M.J. Magma ascent rates. In *Minerals, Inclusions and Volcanic Processes*; Putirka, K.D., Tepley III, F.J., Eds.; Reviews in Mineralogy and Geochemistry; Mineralogical Society of America and Geochemical Society: Chantilly, VA, USA, 2008; Volume 69, pp. 241–271.
100. Toramaru, A.; Noguchi, S.; Oyoshihara, S.; Tsune, A. MND (microlite number density) water exsolution rate meter. *J. Volcanol. Geotherm. Res.* **2008**, *175*, 156–167. [CrossRef]
101. Gonnermann, H.M.; Manga, M. Magma ascent in the volcanic conduit. In *Modeling Volcanic Processes: The Physics and Mathematics of Volcanism.*; Fagents, S.A., Gregg, T.K.P., Lopez, R.C., Eds.; Cambridge University Press: Cambridge, UK, 2013; pp. 55–84.
102. Lindstrom, D.P. Experimental Study of the Partitioning of the Transition Metals Between Clinopyroxene and Coexisting Silicate Liquids. Ph.D. Thesis, University of Oregon, Eugene, OR, USA, 1976; p. 188.
103. Ray, G.L.; Shimizu, N.; Hart, S.R. An ion microprobe study of the partitioning of trace elements between clinopyroxene and liquid in the system diopside-albite-anorthite. *Geochim. Cosmochim. Acta* **1983**, *47*, 2131–2140. [CrossRef]
104. Hart, S.R.; Dunn, T. Experimental cpx/melt partitioning of 24 trace elements. *Contrib. Mineral. Petrol.* **1993**, *113*, 1–8. [CrossRef]
105. Forsythe, L.M.; Nielsen, R.L.; Fisk, M.R. High-field-strength element partitioning between pyroxene and basaltic to dacitic magmas. *Chem. Geol.* **1994**, *117*, 107–125. [CrossRef]
106. Gaetani, G.A.; Grove, T.L. Partitioning of rare earth elements between clinopyroxene and silicate melt Crystal-chemical controls. *Geochim. Cosmochim. Acta* **1995**, *59*, 1951–1962. [CrossRef]
107. Lundstrom, C.C.; Shaw, H.F.; Ryerson, F.J.; Phinney, D.L.; Gill, J.B.; Williams, Q. Compositional controls on the partitioning of U, Th, Ba, Pb, Sr and Zr between clinopyroxene and haplobasaltic melts: implications for uranium series disequilibria in basalts. *Earth Planet. Sci. Lett.* **1994**, *128*, 407–423. [CrossRef]
108. Lundstrom, C.C.; Shaw, H.F.; Ryerson, F.J.; Williams, Q.; Gill, J. Crystal chemical control of clinopyroxene-melt partitioning in the Di-Ab-An system: Implications for elemental fractionations in the depleted mantle. *Geochim. Cosmochim. Acta* **1998**, *62*, 2849–2862. [CrossRef]
109. Skulski, T.; Minarik, W.; Watson, E.B. High-pressure experimental trace-element partitioning between clinopyroxene and basaltic melts. *Chem. Geol.* **1994**, *117*, 127–147. [CrossRef]
110. Sun, C.; Liang, Y. Distribution of REE between clinopyroxene and basaltic melt along a mantle adiabat: Effects of major element composition, water, and temperature. *Contrib. Mineral. Petrol.* **2012**, *163*, 807–823. [CrossRef]
111. Yao, L.; Sun, C.; Liang, Y. A parameterized model for REE distribution between low-Ca pyroxene and basaltic melts with applications to REE partitioning in low-Ca pyroxene along a mantle adiabat and during pyroxenite-derived melt and peridotite interaction. *Contrib. Mineral. Petrol.* **2012**, *164*, 261–280. [CrossRef]
112. Blundy, J.D.; Robinson, J.A.C.; Wood, B.J. Heavy REE are compatible in clinopyroxene on the spinel lherzolite solidus. *Earth Planet. Sci. Lett.* **1998**, *160*, 493–504. [CrossRef]
113. Schosnig, M.; Hoffer, E. Compositional dependence of REE partitioning between diopside and melt at 1 atmosphere. *Contrib. Mineral. Petrol.* **1998**, *133*, 205–216. [CrossRef]
114. Bennett, S.L.; Blundy, J.; Elliott, T. The effect of sodium and titanium on crystal-melt partitioning of trace elements. *Geochim. Cosmochim. Acta* **2004**, *68*, 2335–2347. [CrossRef]

115. Marks, M.; Halama, R.; Wenzel, T.; Markl, G. Trace element variations in clinopyroxene and amphibole from alkaline to peralkaline syenites and granites: Implications for mineral-melt trace-element partitioning. *Chem. Geol.* **2004**, *211*, 185–215. [CrossRef]
116. Adam, J.; Green, T. Trace element partitioning between mica-and amphibole-bearing garnet lherzolite and hydrous basanitic melt: 1. Experimental results and the investigation of controls on partitioning behaviour. *Contrib. Mineral. Petrol.* **2006**, *152*, 1–17. [CrossRef]
117. Tuff, J.; Gibson, S.A. Trace-element partitioning between garnet, clinopyroxene and Fe-rich picritic melts at 3 to 7 GPa. *Contrib. Mineral. Petrol.* **2007**, *153*, 369–387. [CrossRef]
118. Francis, D.; Minarik, W. Aluminum-dependent trace element partitioning in clinopyroxene. *Contrib. Mineral. Petrol.* **2008**, *156*, 439–451. [CrossRef]
119. Mollo, S.; Forni, F.; Bachmann, O.; Blundy, J.D.; De Astis, G.; Scarlato, P. Trace element partitioning between clinopyroxene and trachy-phonolitic melts: A case study from the Campanian ignimbrite (Campi Flegrei, Italy). *Lithos* **2016**, *252–253*, 160–172. [CrossRef]
120. Hill, E.; Wood, B.J.; Blundy, J.D. The effect of Ca-Tschermaks component on trace element partitioning between clinopyroxene and silicate melt. *Lithos* **2000**, *53*, 203–215. [CrossRef]
121. Dohmen, R.; Blundy, J. A predictive thermodynamic model for element partitioning between plagioclase and melt as a function of pressure, temperature and composition. *Am. J. Sci.* **2014**, *314*, 1319–1372. [CrossRef]
122. Kneip, H.J.; Liebau, F. Feldspars with trivalent non-tetrahedral cations: Experimental studies in the system $NaAlSi_3O_8$-$CaAl_2Si_2O_8$-$LaAl_3SiO_8$. *Eur. J. Min.* **1994**, *6*, 87–98. [CrossRef]
123. Blundy, J.; Wood, B. Crystal-chemical controls on the partitioning of Sr and Ba between plagioclase feldspar, silicate melts, and hydrothermal solutions. *Geochim. Cosmochim. Acta* **1991**, *55*, 193–209. [CrossRef]
124. Bindeman, I.N.; Davis, A.M.; Drake, M.J. Ion microprobe study of plagioclase-basalt partition experiments at natural concentration levels of trace elements. *Geochim. Cosmochim. Acta* **1998**, *62*, 1175–1193. [CrossRef]
125. Bindeman, I.N.; Davis, A.M. Trace element partitioning between plagioclase and melt: Investigation of dopant influence on partition behavior. *Geochim. Cosmochim. Acta* **2000**, *64*, 2863–2878. [CrossRef]
126. Wood, B.J.; Blundy, J.D. The effect of cation charge on crystal–melt partitioning of trace elements. *Earth Planet. Sci. Lett.* **2001**, *188*, 59–71. [CrossRef]
127. Bédard, J.H. Trace element partitioning in plagioclase feldspar. *Geochim. Cosmochim. Acta* **2006**, *70*, 3717–3742. [CrossRef]
128. Tepley, F.J.; Lundstrom, C.C.; McDonough, W.F.; Thompson, A. Trace element partitioning between high-An plagioclase and basaltic to basaltic andesite melt at 1 atmosphere pressure. *Lithos* **2010**, *118*, 82–94. [CrossRef]
129. Hui, H.; Oshrin, J.G.; Neal, C.R. Investigation into the petrogenesis of Apollo 14 high-Al basaltic melts through crystal stratigraphy of plagioclase. *Geochim. Cosmochim. Acta* **2011**, *75*, 6439–6460. [CrossRef]
130. Sun, C.; Graff, M.; Liang, Y. Trace element partitioning between plagioclase and silicate melt: The importance of temperature and plagioclase composition, with implications for terrestrial and lunar magmatism. *Geochim. Cosmochim. Acta* **2017**, *206*, 273–295. [CrossRef]
131. Blundy, J.; Wood, B. Prediction of crystal-melt partition coefficients from elastic moduli. *Nature* **1994**, *372*, 452–454. [CrossRef]
132. Wood, B.J.; Blundy, J.D. A predictive model for rare earth element partitioning between clinopyroxene and anhydrous silicate melt. *Contrib. Mineral. Petrol.* **1997**, *129*, 166–181. [CrossRef]
133. Forni, F.; Petricca, E.; Bachmann, O.; Mollo, S.; De Astis, G.; Piochi, M. The role of magma mixing/mingling and cumulate melting in the Neapolitan Yellow Tuff caldera-forming eruption (Campi Flegrei, Southern Italy). *Contrib. Mineral. Petrol.* **2018**, *173*, 45. [CrossRef]